

Delamination and recycling of Archaean crust caused by gravitational instabilities

Tim E. Johnson¹, Michael Brown², Boris Kaus^{1,3} & Jill A. VanTongeren⁴

¹Institute for Geoscience, University of Mainz, 55099 Mainz, Germany.

²Department of Geology, University of Maryland, College Park, MD 20742, USA.

³Department of Earth Sciences, University of Southern California, Los Angeles, CA 90089-0740, USA.

⁴Department of Geology & Geophysics, Yale University, New Haven, CT 06511, USA.

Contents:

1. Supplementary notes for Fig. 1a
2. Phase equilibria modelling
3. Geodynamic numerical modelling
4. References

1. Supplementary notes for Fig. 1a

The data used in Fig. 1a are taken from Herzberg *et al.* (2010) with the following corrections to the ages: Coonterunah Group, Pilbara craton, 3.515 Ga (Green *et al.*, 2000, p. 71); Sulfur Springs Group, Pilbara craton, 3.245 Ga (mean of maximum and minimum age constraints in Smithies *et al.*, 2005, Fig. 2); Warrawoona Group Pilbara craton, 3.459 Ga (mean of maximum and minimum age constraints in Kato & Nakamura, 2003, p. 193); Ivisaartoq, Greenland, 3.018 Ga (mean of maximum and minimum age constraints in Polat *et al.*, 2008, p. 297); Iringora structure, north Karelian greenstone belt, Finland, 2.282 Ga (Shchipansky *et al.*, 2004, p.448); Kushtagi-Hungund greenstone belt, India, 2.707 Ga (Balakrishnan *et al.*, 1999, p. 74); Phulad ophiolite, Delhi Supergroup, Rajasthan, India, 1.4 Ga (minimum age, Volpe & Macdougall, 1990, p. 186); Yiyang, South China Block, 0.823 Ga (Wang *et al.*, 2007, p. 1104); Chukotat Group, Cape Smith belt, Canada (mean of maximum and minimum age constraints in St. Onge *et al.*, 1999, Fig. 3); Nathdwara, Aravalli Supergroup, India, 2.3 Ga (Ahmad *et al.*, 2008, p. 155); Vermillion greenstone belt, Minnesota, USA, 2.7 Ga (Card, 1990).

2. Phase equilibria modelling

The phase equilibria modelling uses primary melt compositions calculated by inversion of the major element chemistry of non-arc basalts of varying age as a proxy for the changing composition of the primary crust and by mass balance its complementary residue with time

(Herzberg *et al.*, 2010). The results are presented as isothermal (temperature = 1000 or 900 °C) pressure (P) – composition (X) pseudosections calculated in the Na₂O–CaO–K₂O–FeO–MgO–Al₂O₃–SiO₂–H₂O–TiO₂–O₂ (NCKFMASHTO) chemical system for the primary melt compositions and the CaO–FeO–MgO–Al₂O₃–SiO₂–O₂ (CFMASO) chemical system for the complementary residue compositions. Calculation were performed using *Perple_X* (Connolly, 2005) and the internally consistent thermodynamic dataset of Holland & Powell (1998) with the following activity–composition models for solid-solution phases: garnet (White *et al.* 2007), clinopyroxene and amphibole (Diener & Powell, 2012), orthopyroxene and spinel–magnetite (White *et al.*, 2002), plagioclase (Holland & Powell, 2003), and ilmenite–hematite (White *et al.*, 2000). FMS olivine incorporates a symmetric Fe–Mg interaction parameter ($W_{fo,fa}$) of 8 kJ.

The primary crust is modelled either as fully hydrated, requiring < or <<1.5 wt% H₂O, in which H₂O is contained within hornblende with ~2 wt% H₂O, or as anhydrous, whereas the residues are modelled as anhydrous. The hydrated and anhydrous end-member cases allow consideration of variable hydration of the primary crust. The modelled compositional range for primary crust is a binary mixture between the primary melt composition for MORB ($X = 0$) and a fictive end member composition (MgO of 25 wt%; $X = 1$) as a proxy for primary crust generated at extreme T_p (Herzberg *et al.*, 2010; Fig. 1b). The composition of these end members in terms of the components SiO₂, TiO₂, Al₂O₃, FeO, MgO, CaO, Na₂O, O₂ expressed as mol.% and normalised to 100% is: 49.49, 0.66, 10.11, 6.69, 17.72, 12.72, 2.28, 0.33 ($X = 0$) and 42.96, 0.60, 2.61, 10.09, 34.97, 7.53, 0.99, 0.25 ($X = 1$). The end member compositions of the binary compositional range for the complementary residue in terms of the components SiO₂, Al₂O₃, FeO, MgO, CaO, O₂ expressed as mol.% and normalised to 100% is: 38.25, 1.61, 5.80, 51.66, 2.53, 0.15 ($X = 0$) and 35.76, 1.28, 4.07, 58.52, 0.27, 0.10 ($X = 1$). All calculations use a constant Fe³⁺/(Fe³⁺ + Fe²⁺) ratio of 0.1 (Berry *et al.*, 2008). The model calculation and phase diagrams include the following phases (and abbreviations): olivine (ol), garnet (g), clinopyroxene (cpx), orthopyroxene (opx), hornblende (hb), plagioclase (pl), quartz (q), ilmenite (ilm), rutile (ru), spinel (sp), magnetite (mt), hematite (hem) and H₂O as appropriate.

Figure 2 shows the hydrated (Fig. 2a) and anhydrous (Fig. 2b) metamorphic mineral assemblage stability fields for the range of primary melt compositions (from $X = 0$ to $X = 1$) and their complementary residues, Fig. 2c, for pressure up to 3.5 GPa at 1000 °C; also shown in Fig. 2a is the reduced stability field of amphibolite at 900 °C. These simplified diagrams are based on the complete phase diagrams shown in Figs S1a–S6a and the rock names used in Fig. 2 are based on the modes shown in Figs S1b–S6b, which are located at the end of this section. In Figs 2a, b, the green field of amphibolite and garnet amphibolite is defined by assemblages containing both hornblende and plagioclase. Ultramafic rocks shown in blue are defined by assemblages lacking plagioclase but containing diopsidic clinopyroxene ($X_{jd} < 0.20$), within which metahornblendites contain >50 vol.% hornblende. In the purple eclogite field garnet and omphacitic clinopyroxene ($X_{jd} > 0.25$) coexist with rutile and quartz/coesite. ‘Eclogitic’ rocks in pale purple are modally dominated by garnet and clinopyroxene of ‘intermediate’ composition ($0.20 < X_{jd} < 0.25$). For primary crust at 1000 °C, clinopyroxene abundance varies widely from <15 to >50 vol.%, but is predicted in all assemblages; it is diopside except at high P (>1.8 GPa) and low MgO (<15 wt%), where it is omphacite. Hornblende contents are up to 60 vol.%, with maximum abundances at around 1.0 GPa and 18 wt% MgO. Garnet is stable above 1.0 GPa at low MgO and above 1.5 GPa at the highest MgO contents modelled. Low MgO (< 15 wt%) ‘MORB-like’ compositions are amphibolites at ~0.6–1.0 GPa or garnet-amphibolites at ~1.0–1.7 GPa in which rutile is stable at $P > 1.3$

GPa, and anhydrous kyanite-bearing quartz/coesite eclogites at $P > 1.7$ GPa. High MgO compositions (>18 wt%) contain olivine, orthopyroxene and ilmenite at all modelled pressures; they are metahornblendites or metapyroxenites above ~ 0.75 – 0.65 GPa to ~ 2.3 GPa and anhydrous garnet pyroxenites at higher pressure. For intermediate compositions (15–18 wt% MgO) the upper pressure stability limit of plagioclase (and hence amphibolite) declines steeply to lower pressures with increasing MgO. Amphibolites will begin to melt at ~ 900 °C, potentially to produce TTG-like melts. Metahornblendites and hornblende-bearing metapyroxenites will begin to melt at ~ 1000 °C, potentially to produce basalt.

In Fig. 2c all compositions are peridotites with >50 vol.% olivine and 10–30 vol.% orthopyroxene; the abundance of both phases increases with increasing MgO. Garnet-harzburgite with trace amounts of clinopyroxene is predicted in all but the lowest MgO compositions at $P > 1.25$ GPa; spinel-bearing peridotites are stable at $P < 1.2$ and additionally contain plagioclase at $P < 0.8$ GPa. Lherzolite with > 5 vol.% clinopyroxene is only stable in relatively low MgO residues and at $P < 1.5$ GPa (because the degrees of melting are lower in this X–P range). Also shown are contours for the forsterite content of olivine (as $Mg\# = 100 * \text{molar MgO}/(\text{MgO} + \text{FeO})$), which increases from 91 to 94 with increasing MgO.

Figures 3a and b show the calculated densities for hydrated and anhydrous primary crust calculated at 1000 °C, whereas Fig. 3c shows the calculated densities for the complementary residues, plotted against MgO of the primary crust. The densities shown in these diagrams are based on the complete phase diagrams shown in Figs S1a, S3a and S5a. The residues have densities ranging from < 3200 kg/m³ at low P to > 3360 kg/m³ at 3.5 GPa for low MgO compositions. At fixed pressure, densities decrease with increasing MgO by up to 2% across the full compositional range modelled. Density contours for the metamorphosed primary crust are more complex reflecting the more variable mineral assemblages. For both fully hydrated and anhydrous primary crust the lowest densities occur at low P and low MgO where the calculated abundance of plagioclase is highest. At low pressures (< 1.0 GPa), densities increase towards higher MgO and, at fixed pressure, may increase by 8% over the full compositional range modelled. In fully hydrated primary crust at low MgO compositions, density increases dramatically between 1.0 and 2.0 GPa recording the transition from amphibolite to eclogite. In higher MgO compositions densities increase less dramatically with increasing pressure, recording a transition from garnet-absent to garnet-bearing metahornblendite and metapyroxenite and eventually to anhydrous garnet metapyroxenite. In anhydrous primary crust at $MgO > 15$ wt% density increases dramatically from ~ 1.0 to > 1.3 GPa recording the appearance of spinel and garnet at the expense of plagioclase, and at $MgO < 15$ wt% density continues to increase to > 2 GPa as plagioclase is eliminated over a wide range of pressure. Figures S7a and b show the calculated densities for hydrated and anhydrous primary crust calculated at 900 °C, whereas Fig. S7c shows the calculated densities for the complementary residues, plotted against MgO of the primary crust. The densities shown in these diagrams are based on the complete phase diagrams shown in Figs S2a, S4a and S6a. The changes in density from 1000 to 900 °C are relatively small. Figure 3d shows the relative density of the metamorphosed fully hydrated primary crust with respect to the underlying residual mantle at 1000 °C plotted against MgO of the primary crust with the equality line for anhydrous crust at 1000 °C and those for 900 °C (based on Supplementary Fig. S7d) superimposed. The solid (hydrated) and dashed (anhydrous) lines separate stable primary crust (below) from potentially unstable primary crust (above).

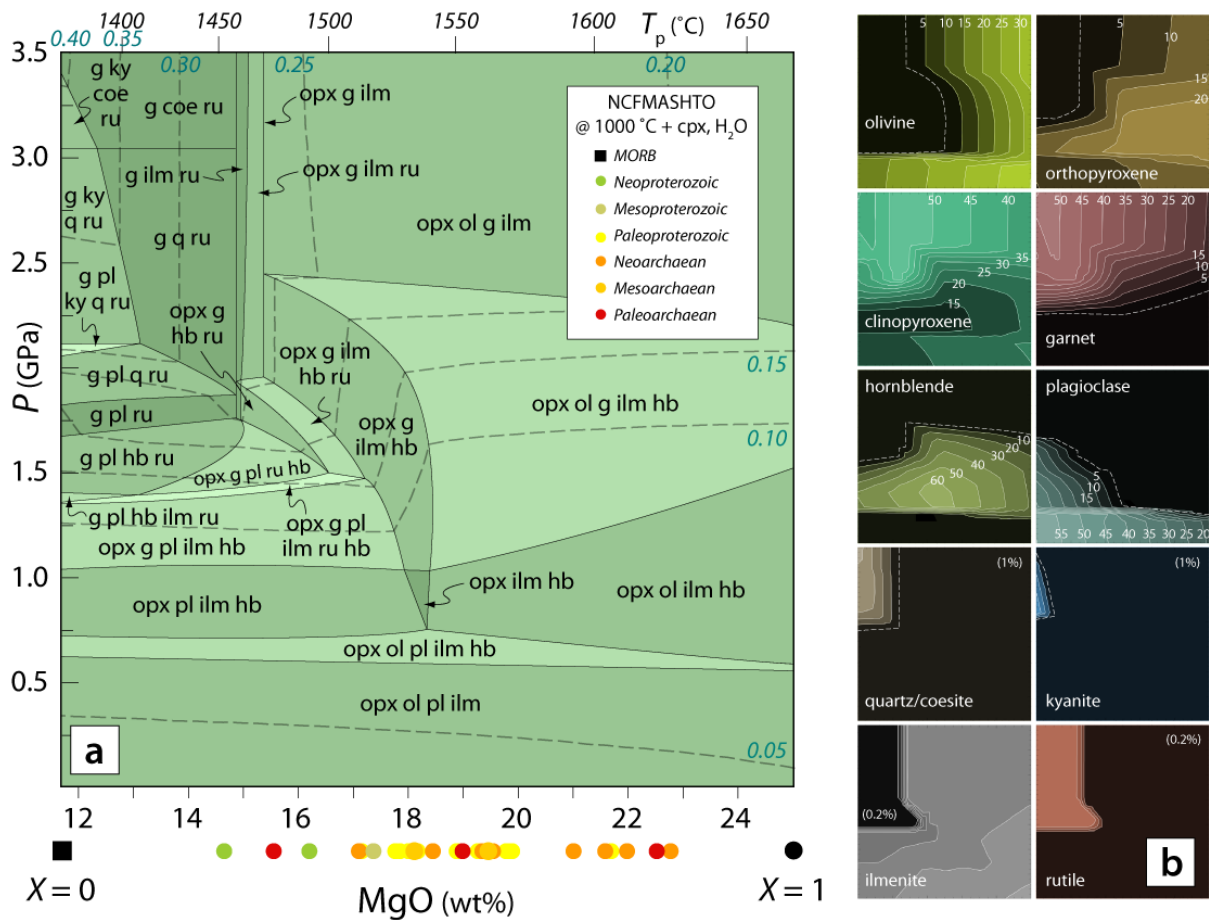


Figure S1. a, Calculated isothermal ($T = 1000\text{ °C}$) P - X pseudosection in the NCFMASHTO chemical system showing the equilibrium (minimum Gibb's free energy) mineral assemblages developed within hydrated primary crust ranging in pressure from 0–3.5 GPa and in composition from the calculated primary melt composition of MORB ($X = 0$) to a fictive end member with 25 wt% MgO ($X = 1$), together with the equivalent mantle potential temperatures (T_p ; Herzberg *et al.*, 2010). The extrapolated peak pressures at 1000 °C based on the apparent thermal gradients recorded by metamorphosed Precambrian rocks are also shown (Brown, 2007). The pseudosection is contoured for the mole fraction of the jadeite component in clinopyroxene (dashed lines). All fields are H_2O -saturated and all contain clinopyroxene in addition to those minerals listed on the diagram. Abbreviations for modelled phases are as follows: olivine (ol), garnet (g), clinopyroxene (cpx), orthopyroxene (opx), hornblende (hb), plagioclase (pl), quartz (q), ilmenite (ilm), rutile (ru), spinel (sp), magnetite (mt), hematite (hem) and H_2O . The depth of shading of the assemblage fields reflects increasing variance; the palest fields have a variance of 3. All phase diagrams were calculated using the software *Perple_X* (Connolly, 2005). Calculations use the ds55 internally consistent thermodynamic dataset (Holland & Powell, 1998) and the most recently calibrated activity–composition models (Diener & Powell, 2012). **b**, Calculated modal abundance (in vol.%) of phases within the modelled primary crust. The pressures and binary compositional range are the same as in a. The intervals between vol.% contours for the minor phases quartz/coesite, kyanite, ilmenite and rutile are indicated.

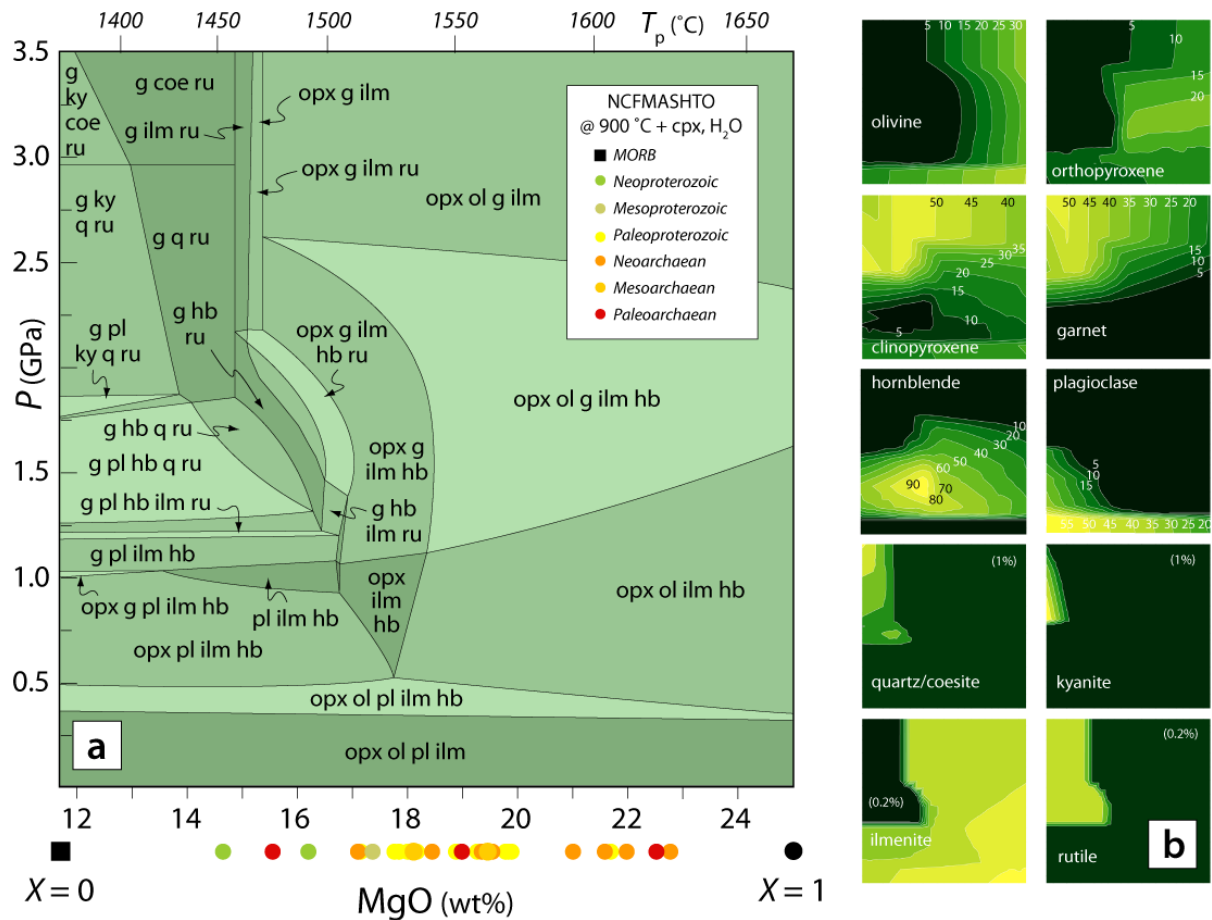


Figure S2. a, Calculated isothermal ($T = 900\text{ °C}$) P - X pseudosection in the NCFMASHTO chemical system showing the equilibrium (minimum Gibb's free energy) mineral assemblages developed within hydrated primary crust ranging in pressure from 0–3.5 GPa and in composition from the calculated primary melt composition of MORB ($X = 0$) to a fictive end member with 25 wt% MgO ($X = 1$), together with the equivalent mantle potential temperatures (T_p ; Herzberg *et al.*, 2010). The extrapolated peak pressures at 1000 °C based on the apparent thermal gradients recorded by metamorphosed Precambrian rocks are also shown (Brown, 2007). All fields are H_2O -saturated and all contain clinopyroxene in addition to those minerals listed on the diagram. Abbreviations for modelled phases are as follows: olivine (ol), garnet (g), clinopyroxene (cpx), orthopyroxene (opx), hornblende (hb), plagioclase (pl), quartz (q), ilmenite (ilm), rutile (ru), spinel (sp), magnetite (mt), hematite (hem) and H_2O . The depth of shading of the assemblage fields reflects increasing variance; the palest fields have a variance of 3. All phase diagrams were calculated using the software *Perple_X* (Connolly, 2005). Calculations use the ds55 internally consistent thermodynamic dataset (Holland & Powell, 1998) and the most recently calibrated activity–composition models (Diener & Powell, 2012). **b**, Calculated modal abundance (in vol.%) of phases within the modelled primary crust. The pressures and binary compositional range are the same as in a. The intervals between vol.% contours for the minor phases quartz/coesite, kyanite, ilmenite and rutile are indicated.

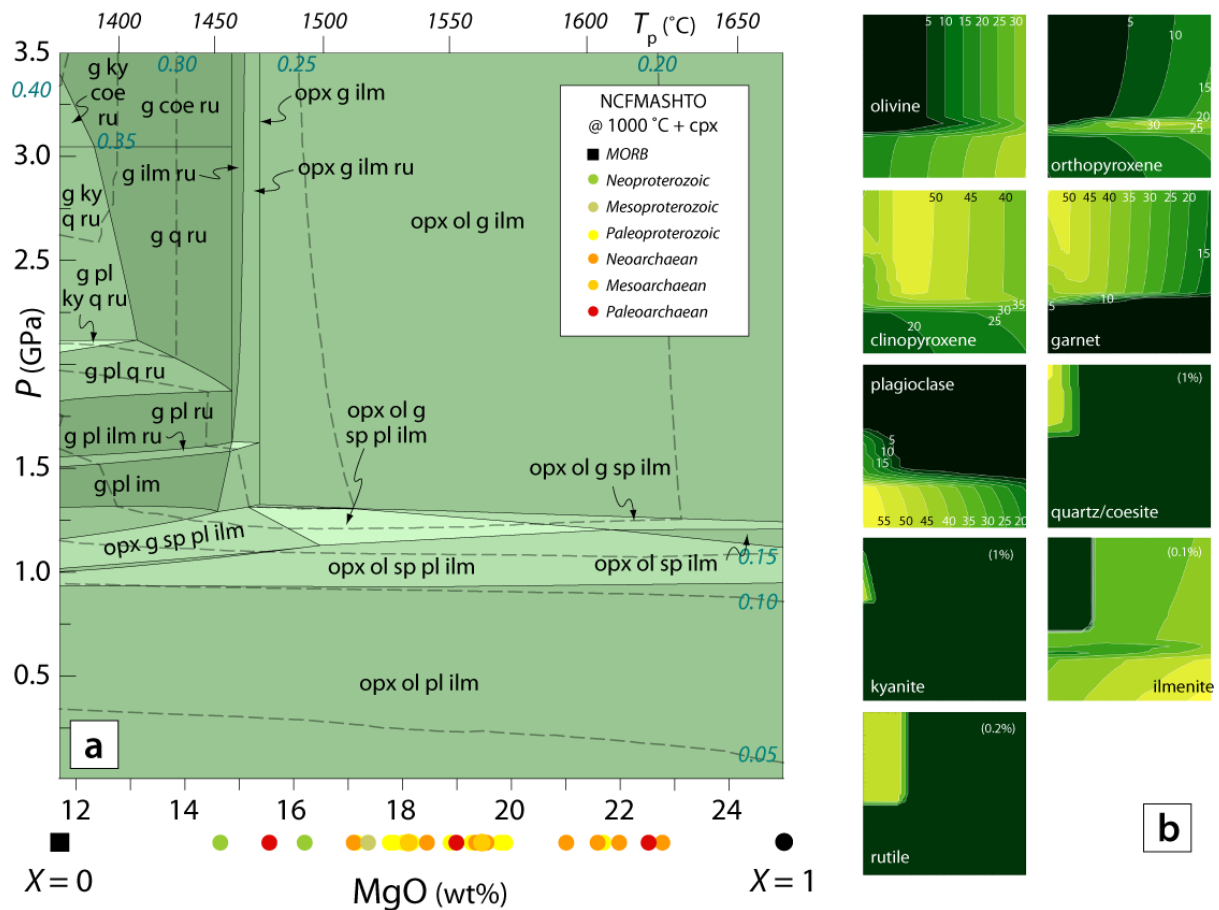


Figure S3. a, Calculated isothermal ($T = 1000\text{ °C}$) P - X pseudosection in the NCFMASHTO chemical system showing the equilibrium (minimum Gibbs free energy) mineral assemblages developed within anhydrous primary crust ranging in pressure from 0–3.5 GPa and in composition from the calculated primary melt composition of MORB ($X = 0$) to a fictive end member with 25 wt% MgO ($X = 1$), together with the equivalent mantle potential temperatures (T_p ; Herzberg *et al.*, 2010). The extrapolated peak pressures at 1000 °C based on the apparent thermal gradients recorded by metamorphosed Precambrian rocks are also shown (Brown, 2007). All fields contain clinopyroxene in addition to those minerals listed on the diagram. Abbreviations for modelled phases are as follows: olivine (ol), garnet (g), clinopyroxene (cpx), orthopyroxene (opx), plagioclase (pl), quartz (q), ilmenite (ilm), rutile (ru), spinel (sp), magnetite (mt), and hematite (hem). The depth of shading of the assemblage fields reflects increasing variance; the palest fields have a variance of 3. All phase diagrams were calculated using the software *Perple_X* (Connolly, 2005). Calculations use the *ds55* internally consistent thermodynamic dataset (Holland & Powell, 1998) and the most recently calibrated activity–composition models (Diener & Powell, 2012). **b**, Calculated modal abundance (in vol.%) of phases within the modelled primary crust. The pressures and binary compositional range are the same as in a. The intervals between vol.% contours for the minor phases quartz/coesite, kyanite, ilmenite and rutile are indicated.

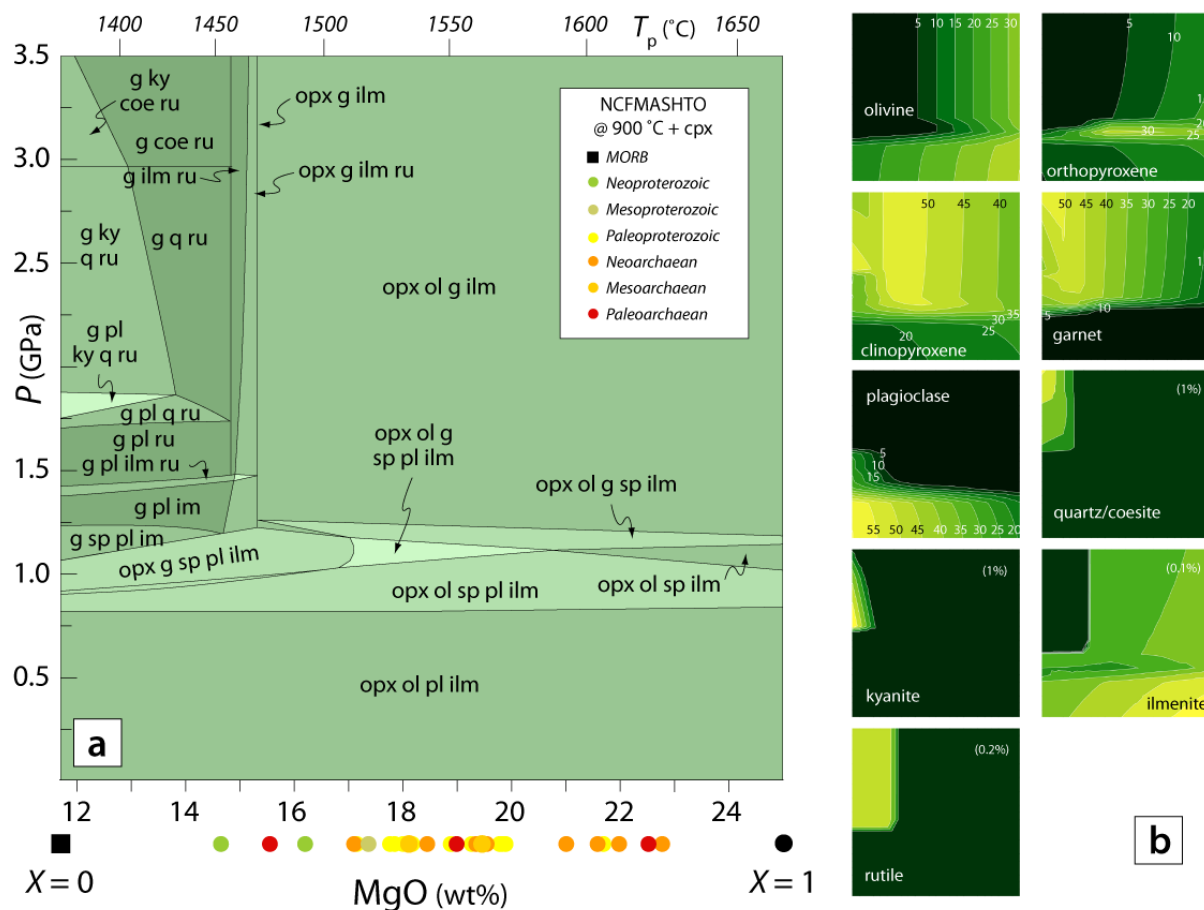


Figure S4. a, Calculated isothermal ($T = 900\text{ °C}$) P - X pseudosection in the NCFMASHTO chemical system showing the equilibrium (minimum Gibb's free energy) mineral assemblages developed within hydrated primary crust ranging in pressure from 0–3.5 GPa and in composition from the calculated primary melt composition of MORB ($X = 0$) to a fictive end member with 25 wt% MgO ($X = 1$), together with the equivalent mantle potential temperatures (T_p ; Herzberg *et al.*, 2010). The extrapolated peak pressures at 1000 °C based on the apparent thermal gradients recorded by metamorphosed Precambrian rocks are also shown (Brown, 2007). All fields contain clinopyroxene in addition to those minerals listed on the diagram. Abbreviations for modelled phases are as follows: olivine (ol), garnet (g), clinopyroxene (cpx), orthopyroxene (opx), plagioclase (pl), quartz (q), ilmenite (ilm), rutile (ru), spinel (sp), magnetite (mt), and hematite (hem). The depth of shading of the assemblage fields reflects increasing variance; the palest fields have a variance of 3. All phase diagrams were calculated using the software *Perple_X* (Connolly, 2005). Calculations use the ds55 internally consistent thermodynamic dataset (Holland & Powell, 1998) and the most recently calibrated activity–composition models (Diener & Powell, 2012). **b**, Calculated modal abundance (in vol.%) of phases within the modelled primary crust. The pressures and binary compositional range are the same as in a. The intervals between vol.% contours for the minor phases quartz/coesite, kyanite, ilmenite and rutile are indicated.

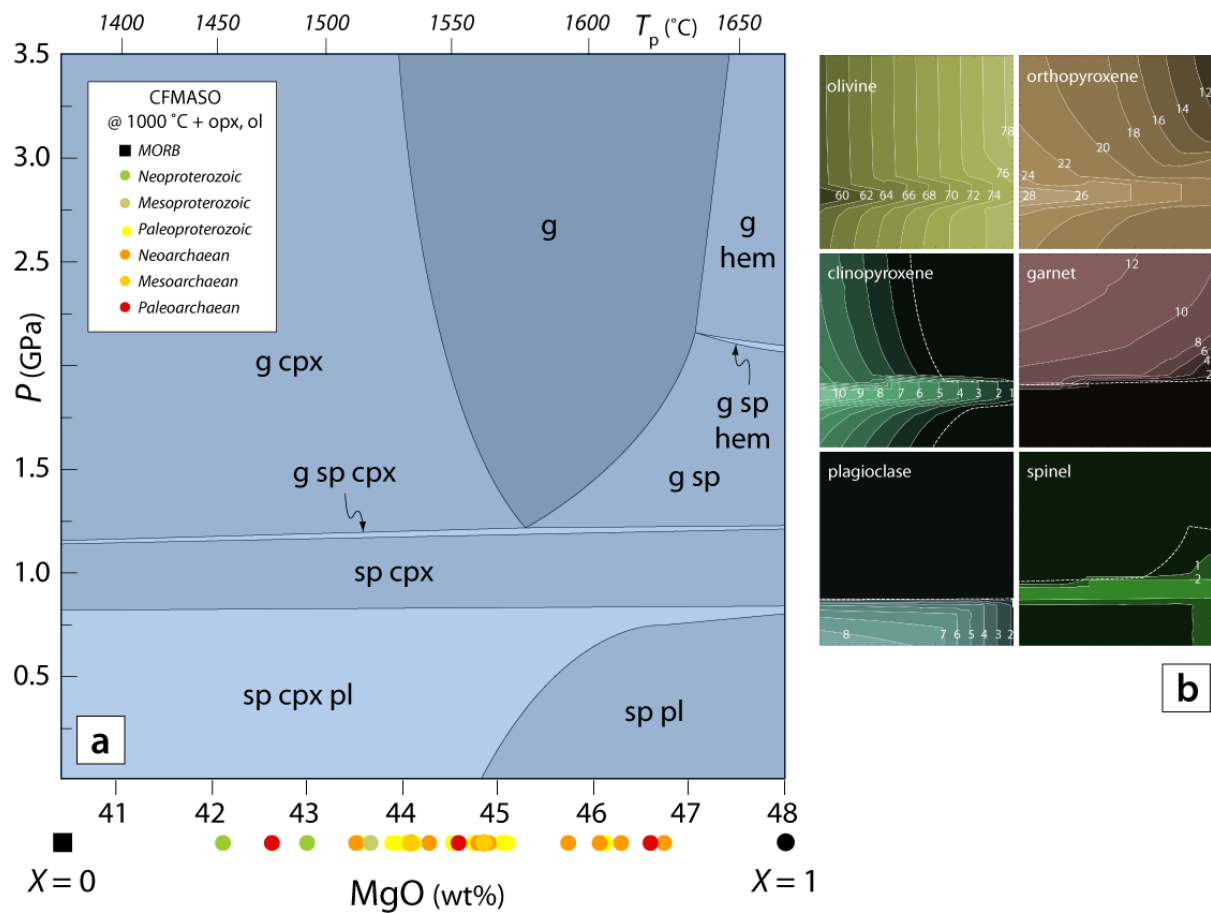


Figure S5. **a**, Calculated isothermal ($T = 1000\text{ °C}$) P - X pseudosection in the CFMASO chemical system showing the equilibrium (minimum Gibb's free energy) mineral assemblages developed within mantle residues ranging in pressure from 0–3.5 GPa and in composition from the calculated residue composition of MORB ($X = 0$) to that of a fictive end member with 48 wt% MgO ($X = 1$), together with the equivalent mantle potential temperatures (T_p ; Herzberg *et al.*, 2010). The extrapolated peak pressures at 1000 °C based on the apparent thermal gradients recorded by metamorphosed Precambrian rocks are also shown (Brown, 2007). All fields contain orthopyroxene and olivine in addition to those minerals listed on the diagram. Abbreviations for modelled phases are as follows: garnet (g), clinopyroxene (cpx), plagioclase (pl), and hematite (hem). The depth of shading of the assemblage fields reflects increasing variance; the palest fields have a variance of 4. All phase diagrams were calculated using the software *Perple_X* (Connolly, 2005). Calculations use the ds55 internally consistent thermodynamic dataset (Holland & Powell, 1998) and the most recently calibrated activity–composition models (Diener & Powell, 2012). **b**, Calculated modal abundance (in vol.%) of phases within the modelled mantle residues. The pressures and binary compositional range are the same as in **a**.

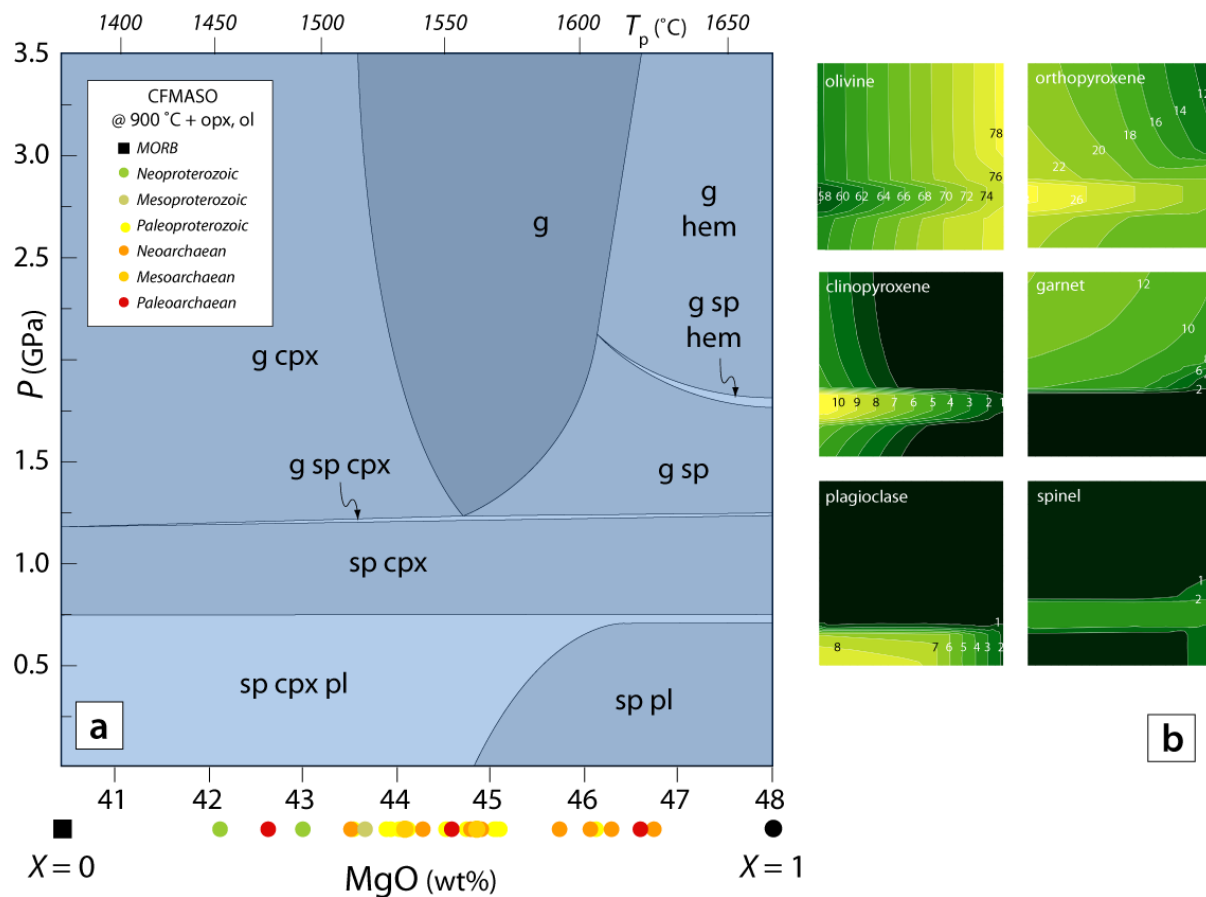


Figure S6. a, Calculated isothermal ($T = 900\text{ °C}$) P - X pseudosection in the CFMASO chemical system showing the equilibrium (minimum Gibbs free energy) mineral assemblages developed within mantle residues ranging in pressure from 0–3.5 GPa and in composition from the calculated residue composition of MORB ($X = 0$) to that of a fictive end member with 48 wt% MgO ($X = 1$), together with the equivalent mantle potential temperatures (T_p ; Herzberg *et al.*, 2010). The extrapolated peak pressures at 1000 °C based on the apparent thermal gradients recorded by metamorphosed Precambrian rocks are also shown (Brown, 2007). All fields contain orthopyroxene and olivine in addition to those minerals listed on the diagram. Abbreviations for modelled phases are as follows: garnet (g), clinopyroxene (cpx), plagioclase (pl), and hematite (hem). The depth of shading of the assemblage fields reflects increasing variance; the palest fields have a variance of 4. All phase diagrams were calculated using the software *Perple_X* (Connolly, 2005). Calculations use the ds55 internally consistent thermodynamic dataset (Holland & Powell, 1998) and the most recently calibrated activity–composition models (Diener & Powell, 2012). **b,** Calculated modal abundance (in vol.%) of phases within the modelled mantle residues. The pressures and binary compositional range are the same as in a.

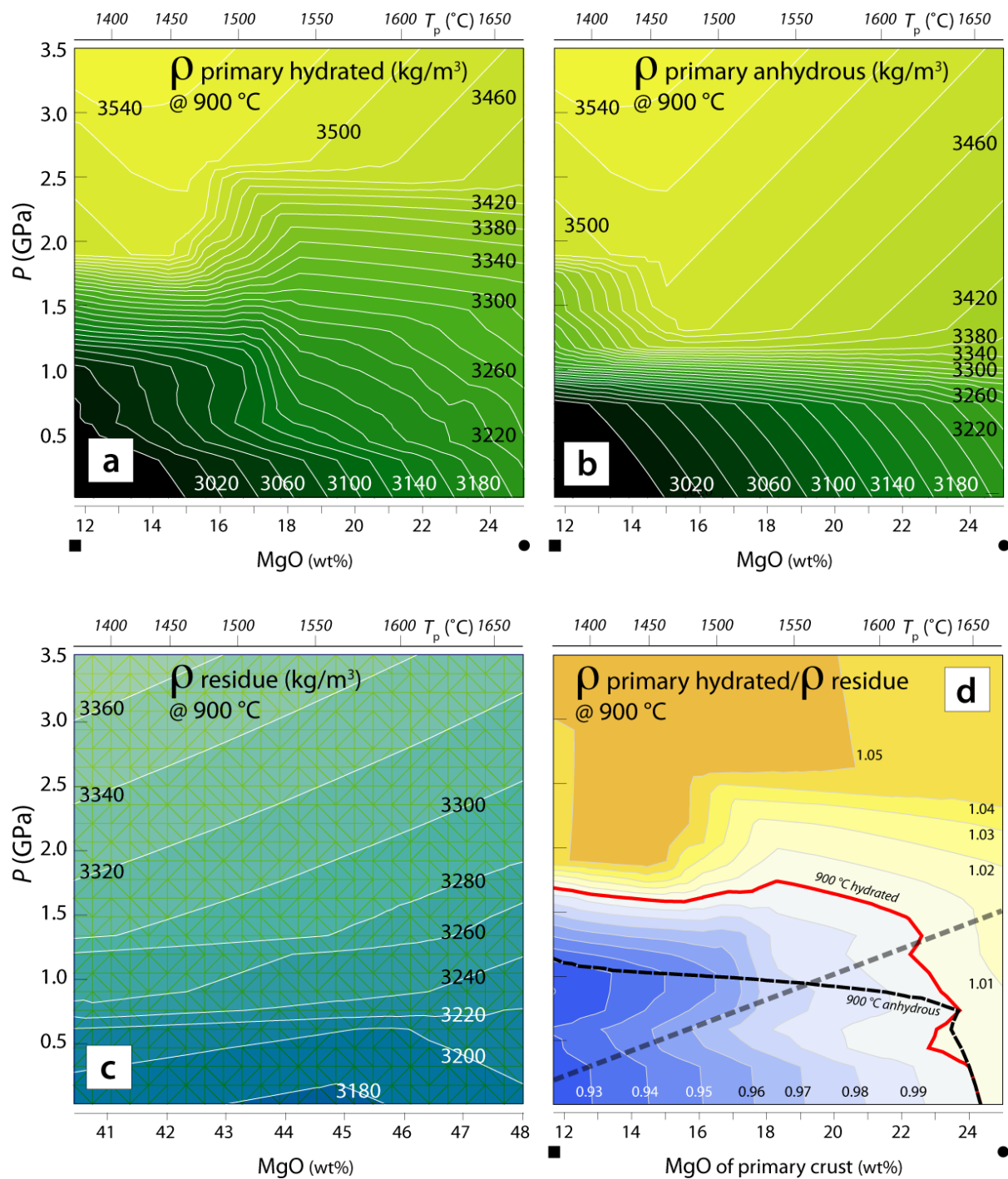


Figure S7. Density of primary crust and complementary residues. Densities calculated at 900 °C plotted against MgO content for **a**, hydrated primary crust, **b**, anhydrous primary crust and **c**, the complementary residues. **d**, Shows the relative density of hydrated crust compared to the underlying residual mantle at 900 °C against MgO of the primary crust with the equality line for anhydrous crust at 900 °C superimposed. The solid (hydrated) and dashed (anhydrous) lines separate stable primary crust (below) from potentially unstable primary crust (above).

3. Geodynamic numerical modelling

3.1. Background

The numerical code employed for the geodynamic simulations has been described in detail elsewhere (Kaus, 2010; Thielmann & Kaus, 2012; Schmeling *et al.*, 2008). For completeness, a brief summary is provided here together with a description of several new features added to the code for the present study, namely melt extraction and evolution.

3.1.1. Governing equations and numerical approach

The incompressible Stokes system of equations are given by

$$\frac{\partial v_i}{\partial x_i} = 0$$

$$-\frac{\partial P}{\partial x_i} + \frac{\partial \tau_{ij}}{\partial x_j} = \rho g_i$$

$$\rho c_p \left(\frac{\partial T}{\partial t} + v_i \frac{\partial T}{\partial x_i} \right) = \frac{\partial}{\partial x_i} \left(k \frac{\partial T}{\partial x_i} \right) + \tau_{ij} \dot{\epsilon}_{ij} - \alpha T \rho g v_2$$

Where v_i indicates velocity, P pressure, τ_{ij} deviatoric stresses, g_i gravitational acceleration, ρ density, c_p heat capacity, T temperature, k thermal conductivity, ϵ_{ij} strain rate, and α thermal expansivity, and the Einstein notation is used and both shear heating and adiabatic (de)compression are taken into account in the energy equation.

Density in the models is a function of rock type/composition (X), melt fraction (M), pressure (P) and temperature (T):

$$\rho = f(X, M, P, T)$$

A viscoplastic constitutive relationship is used, as follows

$$\tau_{ij} = 2\eta_{eff} \dot{\epsilon}_{ij}$$

$$\eta_{eff} = \min(\eta_{diff}, \eta_{disl}, \eta_{yield})$$

in which the dominant rheology is diffusion creep, dislocation creep or plastic yielding, as given by

$$\eta_{diff} = \eta_{0,diff} \exp \left(Q_{diff} \left(\frac{1}{T} - \frac{1}{873} \right) \right)$$

$$\eta_{disl} = \eta_{0,disl} \left(\frac{\dot{\epsilon}_{II}}{10^{-15}} \right)^{\frac{1}{n}-1} \exp \left(Q_{disl} \left(\frac{1}{T} - \frac{1}{873} \right) \right)$$

$$\eta_{yield} = \frac{\sigma_{yield}}{2\dot{\epsilon}_{II}}$$

where σ_{yield} is the yield stress, ϵ_{II} the second invariant of the strain rate tensor, η_0 the effective viscosity at 873 K and 10^{-15} s^{-1} , n the power law exponent and Q the temperature-dependency of viscosity. For mantle rocks we take diffusion and dislocation creep into account for both “wet” and “dry” end-members whereas the crust is assumed to have a diabase dislocation creep rheology. Density depends on the rock-type, melt fraction and the pressure–temperature conditions, as described in more detail below.

The governing equations are solved with the 2D finite element code MILAMIN_VEP, and we employ LBB stable Q₂P₁ elements for the Stokes equations and quadratic elements for temperature. The code is written in MATLAB, but nevertheless is made relatively efficient by employing the techniques described in detail in Dabrowski et al. (2008). Tracers are used to track material properties and the code is used in an ALE mode with regular remeshing to ensure that elements do not become too distorted. This code has been benchmarked for a large number of test problems including convection, Rayleigh-Taylor instabilities, thermal diffusion, shear-heating, and multilayer folding, as well as versus various analytical solutions (e.g. SolCx or weak/strong inclusion setups), as described in a number of publications (Gerya & Yuen, 2007; May & Moresi, 2008; Schmeling *et al.*, 2008; Cramer & Kaus, 2010; Yamato *et al.*, 2011; Cramer *et al.*, 2012; Thielmann & Kaus, 2012).

3.1.2. Phase transitions and partial melting

The variations of crustal density as a function of P and T is computed with *Perple_X*, as described in the main text. We discriminate between initial crust, which has a composition with 23 wt% MgO (at $X = 0.839$ on the binary mixture for the NCFMASHTO modelled primary crust given in the Methods) and “new crust”, which has a composition with 13 wt% MgO (at $X = 0.104$ on the binary mixture for the NCFMASHTO modelled primary crust given in the Methods).

We take into account two types of mantle: lithospheric mantle, which is the residual mantle leftover after forming the initial crust (i.e. it has a composition at $X = 0.839$ on the binary mixture for the CFMASO modelled residua given in the Methods), and underlying asthenospheric mantle, which is more fertile than the lithospheric mantle and has the CFMASO model composition of KR-4003 (Herzberg *et al.* 2010). For both mantle lithologies, initially the density is computed as a function of P and T without melting using *Perple_X*. In a next step, *pMELTS* (Ghiorso *et al.*, 2002) is used to estimate the solidus and liquidus temperatures as well as melt fractions for both (depleted) lithospheric mantle and asthenosphere. Although this gives reliable estimates, *pMELTS* is only well-calibrated for pressures between 1 and 3 GPa and melt fractions smaller than 0.3, whereas the models in this study require information from 0–10 GPa or higher. Therefore, for the fertile asthenospheric mantle the parameterization of Katz *et al.* (2003) is used, but adapted for the appropriate Cpx modal fractions for the composition used. For the more depleted mantle lithosphere, the parameterization of Katz *et al.* (2003) is not well calibrated (as too few

experiments exist), and therefore we rely solely on pMELTS data that have been extrapolated to higher and lower pressures, after adapting the solidus and liquidus parameterization for Katz *et al.* (2003) to fit the pMELTS data in the validity range. In common with most simulations, the lithospheric mantle does not melt extensively; this does not have a large impact on the results of this study, but future experimental work is nevertheless required to better constrain the parameterization.

Melting of crustal rocks is not taken into account in the geodynamic modelling, because a thermodynamic model is not currently available to reliably predict the P – T relations of the solidus and liquidus for these crustal compositions, although, if fully hydrated, one might expect crustal rocks of the compositions modelled in this study to melt above temperatures of 1000 °C. The absence of melting in the crust is a crude first-order approximation. However, we do not expect the inclusion of crustal melting to significantly alter model outcomes because this will produce both melt and residue, and the latter will be even denser than the densities already used, so the drips will likely continue descending into the mantle.

3.1.3. Melting and melt extraction

In reality, melt will be extracted by a variety of mechanisms, such as diking or compaction-driven flow. As these processes mostly happen on a timescale that is significantly smaller than the typical time step employed in the model, we assume that melt in the mantle is extracted instantaneously and emplaced on top of the crust. In doing this the possibility that melt might be trapped in the crust during ascent is ignored, which is justified as both mechanisms will thicken the crust.

The melt extraction algorithm largely follows the approach of Sizova *et al.* (2010), and is done in several steps, as follows.

1) The theoretical melt fraction M_0 of a given rock is computed, which depends on the composition of the rock (asthenosphere or mantle lithosphere), the P – T condition and the melting diagram, which is a lookup table as a function of P, T . In general, melt fractions do not vary linearly between solidus and liquidus, but instead change nonlinearly and in a stepwise manner, for example once Cpx in the rock is consumed (Katz *et al.*, 2003).

2) It is assumed that melt will be extracted once the melt fraction exceeds a critical extraction melt fraction ($M_{extract}$), which is set as 0.05 in this work. After a melt-extraction event, a small amount of non-extractable melt (M_{min}) will remain in the rock, which is here taken as 0.02.

3) The amount of melt that has been extracted is tracked on markers. The amount of melt currently present at each marker takes into account melt that has been extracted from that marker during earlier melt extraction events, and is computed as

$$M = M_0 - \sum_n M_{ext}$$

where $\sum_n M_{ext}$ is the total amount of melt extracted in the previous n melt extraction events.

4) If $M > M_{extract}$, the extractable melt fraction $M_{ext} = M - M_{min}$ moves upwards to create new crust and the remaining melt fraction in the mantle (M) is updated. Simultaneously, the remaining rock will have a reduced volume $1 - M_{ext}$, which is compensated by compaction in the vertical direction. This is computed by interpolating the irregular marker distribution on a regular grid on which the vertical motion due to compaction as well as the thickness of the newly formed crust is calculated for every horizontal grid cell. New markers are randomly inserted in the newly generated crust and existing markers are moved downwards accordingly. The newly formed crust, which typically has a thickness of a few 100 meters, will initially be hot (and have mantle temperature) but will cool rapidly on a timescale smaller than the typical time step used (a few 1000 years). For simplicity, therefore, we assume the temperature of the newly formed crust to be 700 °C. Since the characteristic diffusion time for the new crust is typically smaller than the time step, and the new magma is assumed to be emplaced at the surface where gradients in temperature are large, the precise temperature of the new crust does not have a major impact on the results. This simplification was verified by performing additional calculations in which the emplacement temperature was varied from 20 to 900 °C; these experiments yielded similar results. A more sophisticated approach, in which one would model every magmatic pulse with, for example, a 1-D temperature profile, is expected to have little effect on the key results and was not employed here.

5) If more than a certain amount of melt is extracted from a tracer (M_{max}), the rock is assumed to be depleted and no longer produces melt.

6) The effective density of the remaining partially molten mantle rock is computed according to $\rho = M \rho_{melt} + (1 - M) \rho_{phasediagram}$ where ρ_{melt} is the density of the melt, which is assumed to have a constant value of 2800 kg/m³ for simplicity, although we note this is in good agreement with estimates from pMELTS calculations, and $\rho_{phasediagram}$ is the density taken from the phase diagram without partial melting.

The effective viscosity of a partially molten region depends on the melt fraction in a nonlinear fashion (e.g., Bittner, & Schmeling, 1995; Deubelbeiss *et al.*, 2010). As the mafic melts produced in our model are likely to have had a very low viscosity, similar to that of present-day basaltic melts (on the order of 1 Pa s), and the melting typically occurs in regions of the asthenosphere which already have a low solid viscosity, the effective viscosity of the partially molten rock (with no more than 5 vol.% melt in the experiments) is likely to be lower than cut-off viscosity employed. Therefore, a constant viscosity of 10¹⁸ Pas is assigned to regions that are partially molten.

3.1.4. Model setup

The model consists of a 2D box that is 1000 km wide and 660 km high, and has an initial crust of variable thickness, an underlying depleted mantle lithosphere up to a depth of 100 km, and an underlying fertile asthenosphere. Mechanical boundary conditions are free slip (shear stress free) on the side and top boundaries, and no-slip on the bottom boundary, which mimics a viscosity increase in the lower mantle compared to that of the upper mantle. Thermal boundary conditions are isothermal at the top and bottom (in accordance with the initial geotherm) and flux-free at the side boundaries. As the initial geotherm in the Archaean is uncertain and has evolved dynamically, we use a simplistic approach by assuming it to be initially linear in the crust, with 20 °C at the surface and 1000 °C at the Moho, and linearly increasing below until it intersects the mantle adiabat at a depth of 100 km. The mantle adiabat is computed based on T_p (which is varied in the simulations) and an increase of 0.3

K/km. The temperature condition at the bottom of the model is computed from the mantle adiabat. An overview of model parameters is given in Table S1.

The model employs a computational mesh of 257x257 nodes, which is refined towards the lithosphere, such that there is a resolution of 3.9 km (horizontal) by 2.1 km (vertical) in the lithosphere and 3.9 by 3.2 km below a depth of 330 km. Compositions are tracked on tracers of which there are initially ~0.8 million, which number increases during the simulation as new crust is formed. To initiate convection, random noise with a maximum amplitude of 5 °C is initially added on tracers that are deeper than 130 km. As in any geodynamic model with tracers, the fine scale mixing structure in the mantle that occurs in the later stages of the model is not well resolved and should not be interpreted literally (Tackley & King, 2003). The large-scale features, such as the dripping instabilities at the bottom of the lithosphere, are considered to be robust, as tests with a smaller numerical resolution and fewer particles give similar results.

Earth has a free surface, rather than a free slip upper boundary condition as in the experiments. A simulation with standard parameters and a free surface condition was performed to test the effect of this difference on the model dynamics; the result was that the surface condition had a negligible effect on the model dynamics. Surface topographies are typically less than a kilometre in amplitude.

With the chosen geotherm, the asthenosphere immediately underneath the mantle lithosphere is initially partially molten, which results in the formation of a thin layer of new crust at the onset of the simulation (with thicknesses of 2, 5 and 10 km for simulations with a 45 km thick initial crust and a mantle T_p of 1500, 1550 and 1600 °C, respectively). This is a model artefact as in reality the crust would thicken in a dynamic manner and potentially drip-off at the bottom while growing at the top. Notwithstanding, the subsequent evolution of the models is robust, with new crust preferentially forming above upwellings. Moreover, as shown below, models with thinner initial crust produce similar results. Other modelling choices are possible, such as starting with an initially partially depleted asthenosphere, but this is considered unlikely to change the overall findings of the modelling we report herein.

Parameter	Value	Units
Thermal conductivity k	3	W/m/K
Heat capacity c_p	1050	J/kg/K
Gravitational acceleration g	9.81	m/s ²
Lower cutoff viscosity η_{min}	10 ¹⁸	Pa s
Upper cutoff viscosity η_{max}	10 ²⁴	Pa s
Viscosity partially molten zone $\eta_{moltenZone}$	10 ¹⁸	Pa s
Yield stress σ_{yield}	1000	MPa
Crust¹ : dislocation creep prefactor $\eta_{0,dist}$	2.3x10 ²¹	Pas
Crust¹ : dislocation creep powerlaw exponent n	3.05	-
Crust¹ : temperature dependence of viscosity Q_{dist}	1.09x10 ⁴	K
Wet Mantle² : dislocation creep prefactor $\eta_{0,dist}$	1.08x10 ²³	Pas
Wet Mantle²: dislocation creep powerlaw exponent n	3.5	-
Wet Mantle²: temperature dependence of viscosity Q_{dist}	1.6x10 ⁴	K
Wet Mantle² : diffusion creep prefactor $\eta_{0,diff}$	1.1x10 ²⁹	Pas
Wet Mantle²: diffusion dependence of viscosity Q_{diff}	4.03x10 ⁴	K
Dry Mantle² : dislocation creep prefactor $\eta_{0,dist}$	1.07x10 ²⁴	Pas
Dry Mantle²: dislocation creep powerlaw exponent n	3.5	-
Dry Mantle²: temperature dependence of viscosity Q_{dist}	1.82x10 ⁴	K
Dry Mantle² : diffusion creep prefactor $\eta_{0,diff}$	1.8x10 ³¹	Pas
Dry Mantle²: diffusion dependence of viscosity Q_{diff}	4.5x10 ⁴	K
Minimum leftover melt fraction M_{min}	0.02	-
Extraction limit to extract melt and form new crust $M_{extract}$	0.05	-
Maximum extractable melt fraction from the rocks, before they become depleted (non-meltable) mantle rocks M_{max}	0.5	-

Table S1. Model parameters employed in this work. ¹Rheology for the crust are calculated from experiments for a dry diabase rheology as reported by Carter & Tsenn (1987), ²wet and dry mantle dislocation and diffusion creep parameters are taken from Hirth & Kohlstedt (2003), table 1. We assume C_{OH} of 1000 H/10⁶ Si for wet rheologies and a grainsize of 10 mm for diffusion creep. Density and melt fraction are taken from pre-computed phase diagrams.

3.2. Geodynamic model results

Systematic experiments have been run to test the sensitivity of the key results to changes in crustal thickness, mantle T_p , and mantle rheology (wet vs dry).

3.2.1. Effect of initial crustal thickness

Models with $T_p = 1600$ °C, but with varying crustal thickness for a wet and dry mantle rheology (Figs S8, 9), reveal that the physical mechanism is essentially independent of the assumed initial crustal thickness. For crustal recycling to occur, the crust only needs to be

thickened sufficiently to become negatively buoyant at its base at the same time as it becomes sufficiently weak through heating to drip off.

3.2.2. Effect of mantle potential temperature, Moho temperature and rheology

The effect of changing the mantle T_p for a wet mantle rheology is illustrated in Fig. S10. Higher T_p results in a thicker initial crust and in its more rapid removal. As in the case with $T_p = 1600$ °C, the new crust is ultimately recycled into the mantle where it could partially melt (a process that was not modelled). For $T_p < 1550$ °C, a tiny volume of new crust is formed at the beginning of the model runs but later during the runs partial melting no longer occurs in these experiments, and a stagnant lid mode of convection sets in (note that we did not make an attempt to model plate-like behaviour in this study, which requires the use of much smaller yield stresses).

The same analysis for a dry mantle rheology suggests that recycling of the new crust into the mantle stops at a slightly higher T_p (between 1550 and 1600 °C) in these experiments in comparison to those with the wet mantle rheology, but that nonetheless it is a very efficient mechanism above these temperatures (Fig. S11).

Experiments with the ‘standard’ setup (Fig. 4, main paper) but with different initial Moho temperature yield essentially identical results as the standard model, suggesting that the initial thermal state of the crust is a second-order effect in the experiments (Fig. S12). However, it should be noted that crustal melting is not taken into account – adding this process into the model is likely to have an effect at Moho temperatures larger than 1000 °C.

In all experiments, the mantle lithosphere must be eroded and the initial crust thickened before the lower crust is heated sufficiently to generate a dripping instability. Therefore, most of the drips occur above or in the vicinity of upwelling partially molten zones in the mantle, where the newly generated crust “pushes” the older crust into warmer mantle, where it is negatively buoyant. Simultaneously, the depressed crust is heated, which results in a lower effective viscosity that allows Rayleigh-Taylor drips to form in a relatively rapid manner (in agreement with the scaling analysis shown in 3.2.3) For larger values of T_p , erosion of the mantle lithosphere occurs more efficiently, although the original crust remains present for a longer period of time above regions shielded by any leftover mantle lithosphere. At lower T_p this effect plays a more important role and the high viscosity and relatively low density of the mantle lithosphere stabilizes the crust.

As crustal melting is not taken into account in the experiments, the results of these experiments can be regarded as providing conservative estimates on when crustal recycling occurs. Partial melting of the crust would further increase the overall thickness of the crust, which should enhance the recycling effect.

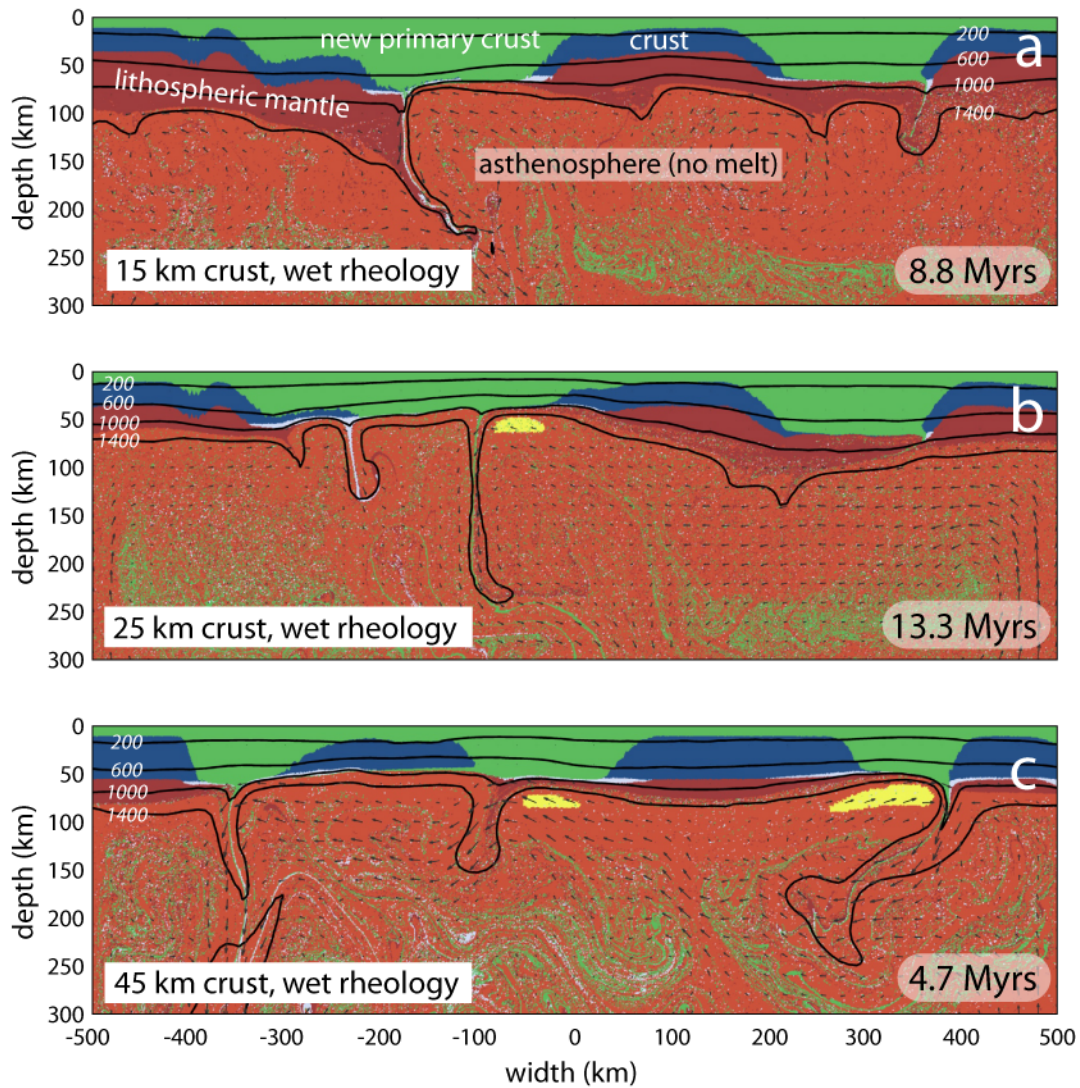


Figure S8. Snapshots from experiments with T_p of 1600 °C and wet mantle rheology. **a**, Initial crustal thickness = 15 km; **b**, initial crustal thickness = 25 km; and, **c**, initial crustal thickness = 45 km. Colours: dark blue, initial primary crust; light blue, negatively buoyant initial primary crust; dark pink-brown, lithospheric mantle; light pink-brown, unmelted asthenosphere; green positively and negatively buoyant newly-created crust; and yellow, melt-bearing asthenosphere).

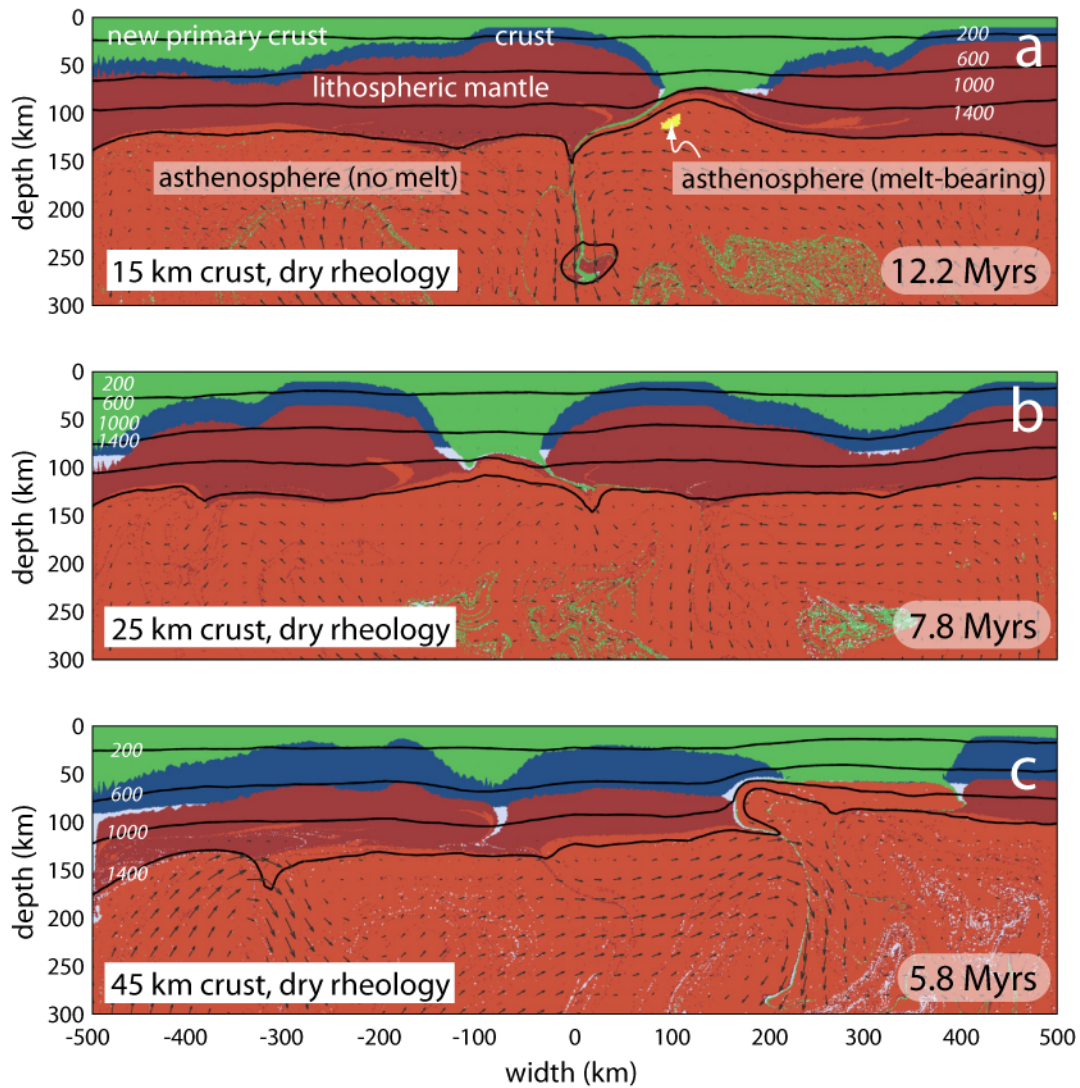


Figure S9. Snapshots from experiments with T_p of 1600 °C and dry mantle rheology. **a**, Initial crustal thickness = 15 km; **b**, initial crustal thickness = 25 km; and, **c**, initial crustal thickness = 45 km. Colours: dark blue, initial primary crust; light blue, negatively buoyant initial primary crust; dark pink-brown, lithospheric mantle; light pink-brown, unmelted asthenosphere; and yellow, melt-bearing asthenosphere).

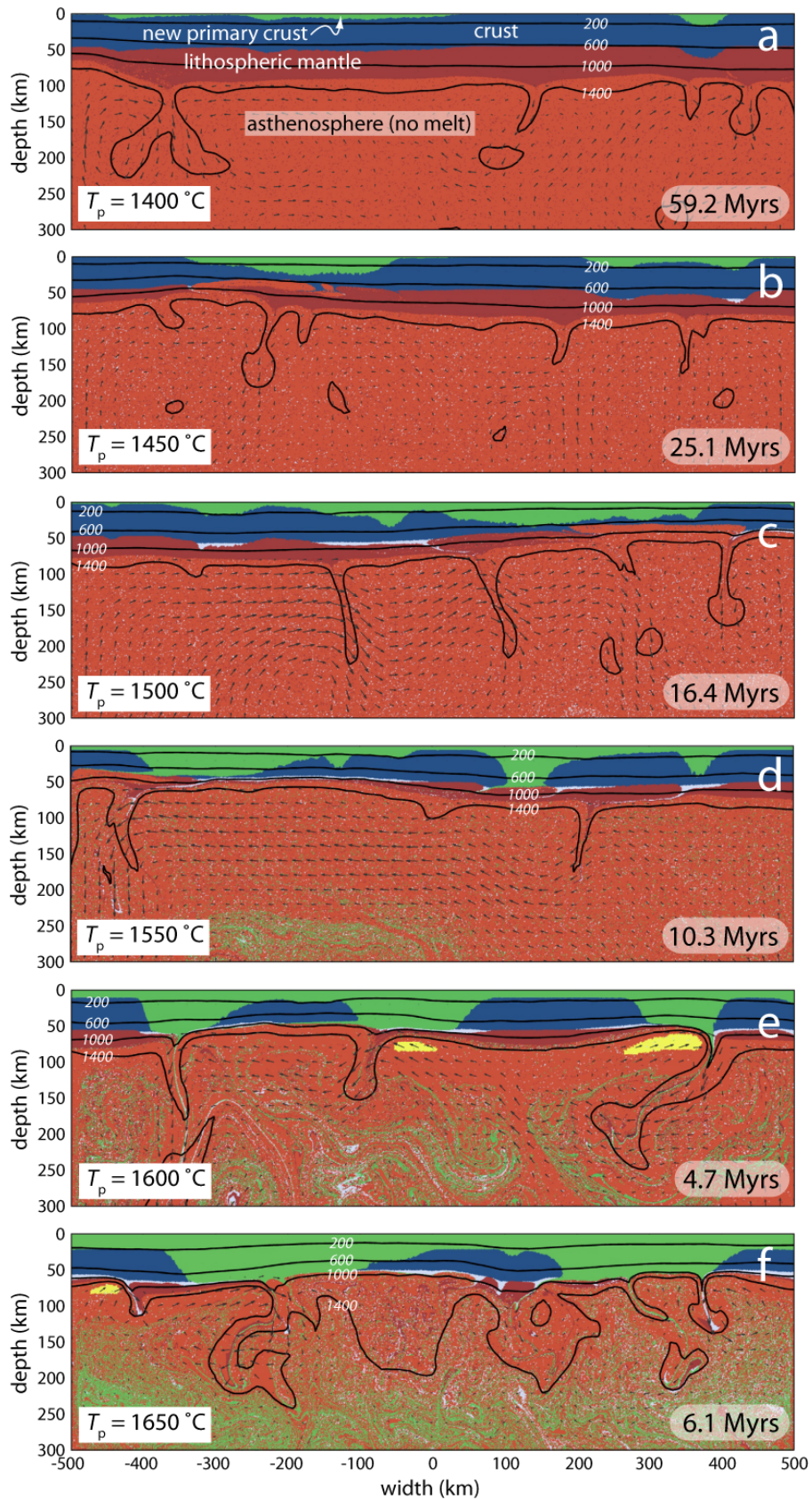


Figure S10. Snapshots from experiments with 45 km thick initial primary crust and wet mantle rheology. **a**, $T_p = 1400\text{ }^\circ\text{C}$; **b**, $T_p = 1450\text{ }^\circ\text{C}$; **c**, $T_p = 1500\text{ }^\circ\text{C}$; **d**, $T_p = 1550\text{ }^\circ\text{C}$; **e**, $T_p = 1600\text{ }^\circ\text{C}$; and, **f**, $T_p = 1650\text{ }^\circ\text{C}$. Colours: dark blue, initial primary crust; light blue, negatively buoyant initial primary crust; dark pink-brown, lithospheric mantle; light pink-brown, unmelted asthenosphere; and yellow, melt-bearing asthenosphere).

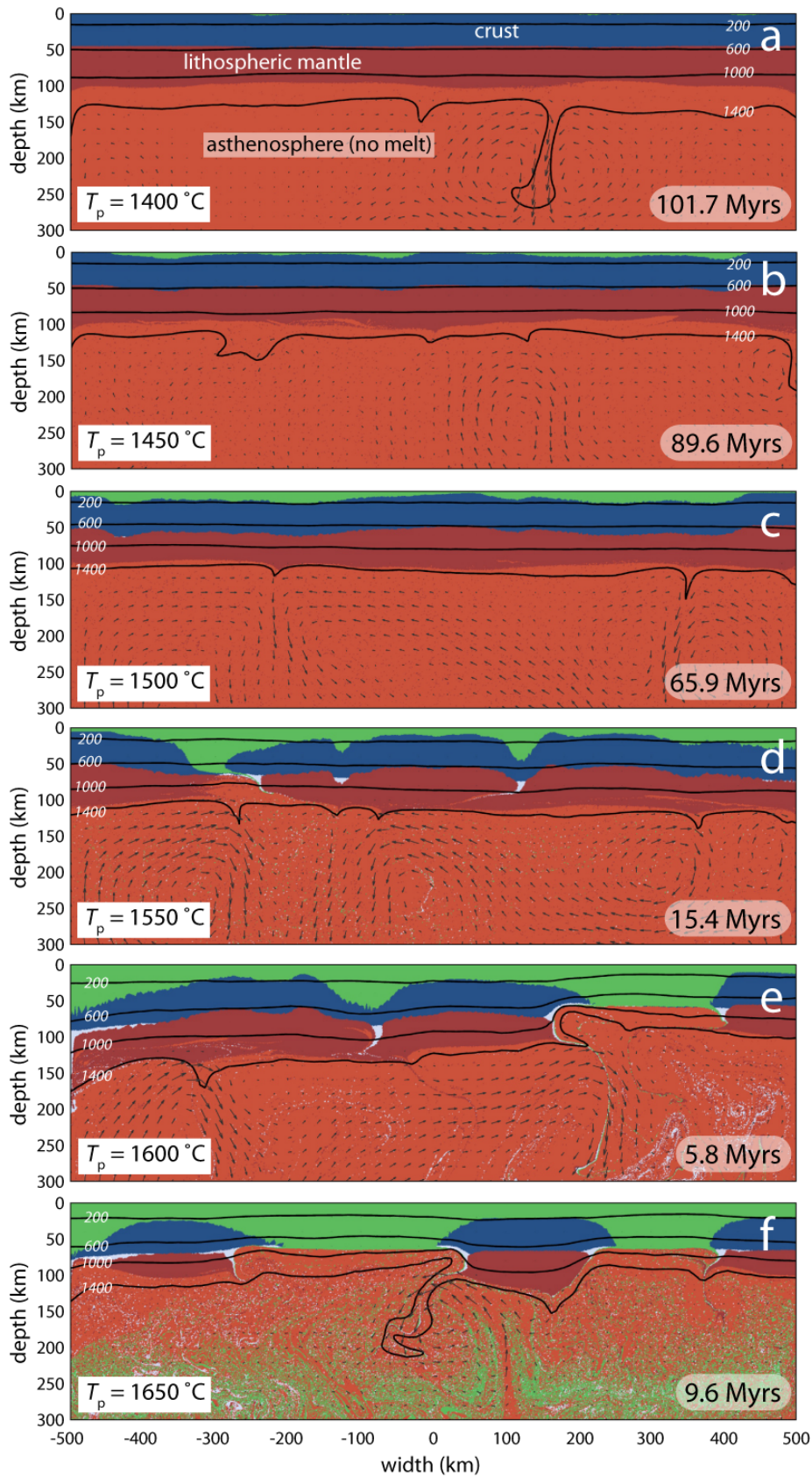


Figure S11. Snapshots from experiments with 45 km thick initial primary crust and dry mantle rheology. **a**, $T_p = 1400\text{ }^\circ\text{C}$; **b**, $T_p = 1450\text{ }^\circ\text{C}$; **c**, $T_p = 1500\text{ }^\circ\text{C}$; **d**, $T_p = 1550\text{ }^\circ\text{C}$; **e**, $T_p = 1600\text{ }^\circ\text{C}$; and, **f**, $T_p = 1650\text{ }^\circ\text{C}$. Colours: dark blue, initial primary crust; light blue, negatively buoyant initial primary crust; dark pink-brown, lithospheric mantle; light pink-brown, unmelted asthenosphere; and yellow, melt-bearing asthenosphere).

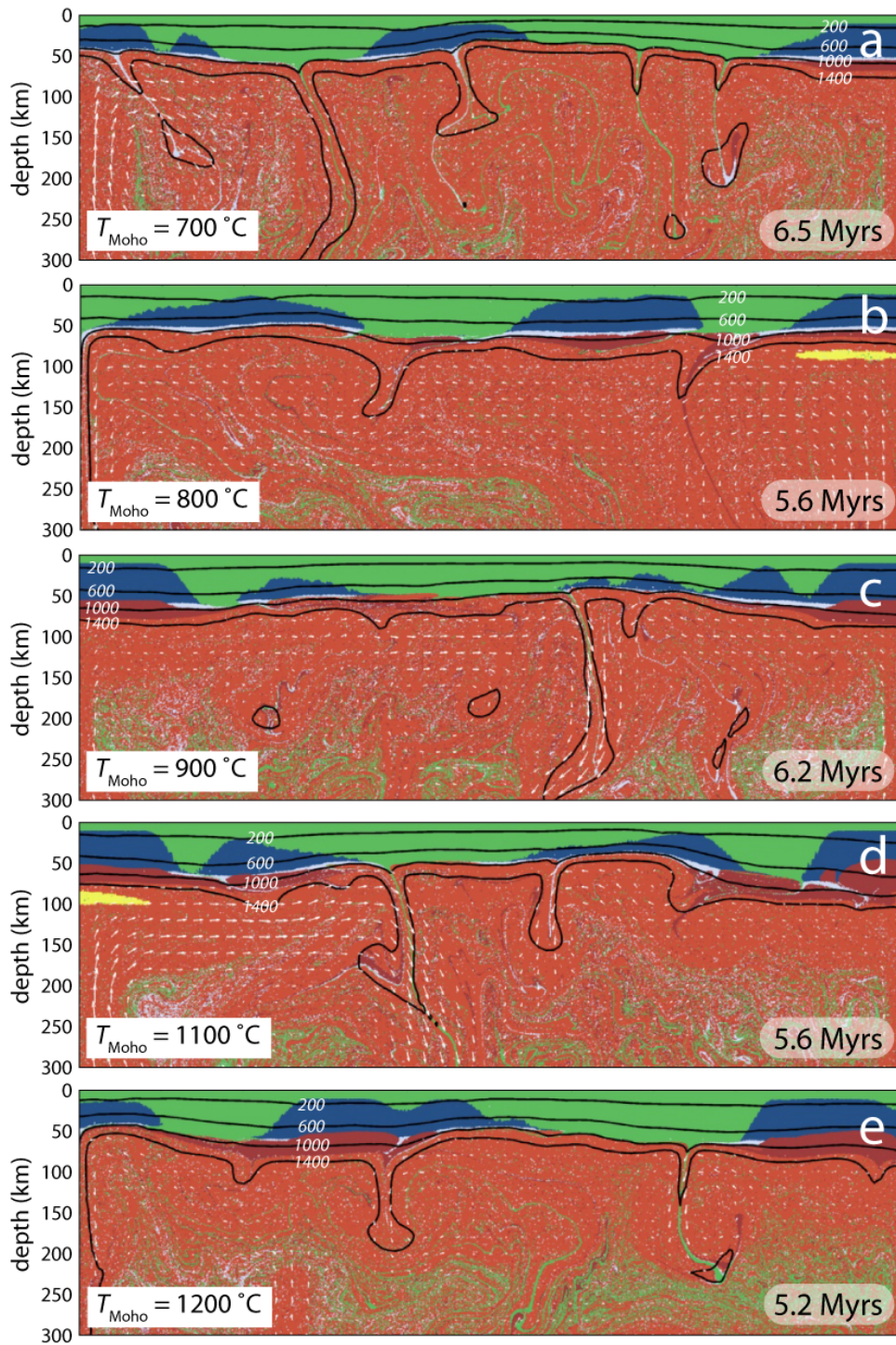


Figure S12. Snapshots from experiments with 45 km thick initial primary crust and wet mantle rheology. **a**, $T_{\text{Moho}} = 700\text{ °C}$; **b**, $T_{\text{Moho}} = 800\text{ °C}$; **c**, $T_{\text{Moho}} = 900\text{ °C}$; **d**, $T_{\text{Moho}} = 1100\text{ °C}$; and, **e**, $T_{\text{Moho}} = 1200\text{ °C}$. Colours: dark blue, initial primary crust; light blue, negatively buoyant initial primary crust; dark pink-brown, lithospheric mantle; light pink-brown, unmelted asthenosphere; and yellow, melt-bearing asthenosphere).

3.2.3. Physics of dripping instabilities

All simulations described above are performed with a hydrous crust, which is a worst-case scenario as the crust becomes negatively buoyant only once it is thickened sufficiently (as described in the main text). We have performed additional simulations with an anhydrous crust, in which almost the full crustal thickness is negatively buoyant. However, since the anhydrous crust is relatively cold, the effective viscosity is too high to allow formation of rapid crustal-scale dripping instabilities. Instead, the experiments behave in a fairly similar manner to those described above in which only parts of the base of the crust drip off, generally above or in the vicinity of upwelling partially molten zones in the mantle.

Insight into the basic physics of the dripping instability is obtained using dimensional analysis. Assuming a layer at the base of the crust with thickness H , it will approximately affect a region of width H and sink with the Stokes sinking velocity, given by

$$V_z \propto \frac{C\Delta\rho g H^2}{\eta}$$

where C is a correction factor, $\Delta\rho$ the average density difference between the crust and the underlying mantle, and η the effective viscosity immediately above or below the Moho.

The characteristic velocity of isotherms due to diffusion is given by

$$V_{diff} \propto \frac{\kappa}{H}$$

For a dripping instability to occur, lateral variations in density should exist, which implies that the instability must grow faster than the characteristic diffusion time (so $t_{adv} > t_d$) otherwise the geotherm at the Moho would be equalized. This results in a non-dimensional critical buoyancy Rayleigh number, given by

$$R_b = \frac{V_z}{V_{diff}} = \frac{C\Delta\rho g H^3}{\eta\kappa}$$

which should be larger than 1 for a dripping instability to occur. Some parameters in this equation are well constrained (namely $\kappa = 10^{-6}$ m²/s, $g = 10$ m/s², $\Delta\rho \sim 50\text{--}200$ kg/m³), whereas others, such as viscosity and layer thickness, are more poorly defined, and C is likely to be a constant based on earlier work (Conrad & Molnar, 1997; Thielmann & Kaus, 2012).

Analysing the numerical experiments at the stage where the dripping instabilities start to form provides a test of the validity of this simple approximation. This task has been undertaken for a number of the experiments in which vertical profiles at the location where a dripping instability occurs were analysed by computing the local thickness and average density difference of the negatively buoyant layer, and determining the maximum viscosity in this region, which generally occurs within the mantle lithosphere. The results of this analysis are summarized in Table S2.

Simulation name	Time [Myrs]	x [km]	Av. $\Delta\rho$ [kg/m ³]	Max η [Pas]	H [km]	T _{moho} [C]	$\Delta\rho g H^3 / (\eta \kappa)$
<i>T_p 1600, Crust 45 km, Wet</i>	1.92	-83	79	5.2x10 ¹⁹	10	996	15.0
<i>T_p 1600, Crust 45 km, Wet</i>	1.92	378	67	4.9x10 ¹⁹	10	986	13.6
<i>T_p 1600, Crust 45 km, Wet</i>	1.97	-320	85	2.5x10 ¹⁹	11	1014	45.6
<i>T_p 1600, Crust 45 km, Wet</i>	2.22	-22	185	1.3x10 ¹⁸	14	1064	3409
<i>T_p 1600, Crust 45 km, Wet</i>	2.20	350	109	1.0x10 ¹⁸	10	1097	1094
<i>T_p 1650, Crust 45 km, Wet</i>	2.61	112	69	3.5x10 ¹⁹	13	994	42.3
<i>T_p 1650, Crust 45 km, Wet</i>	2.56	352	94	3.0x10 ¹⁹	9	964	23.2
<i>T_p 1650, Crust 45 km, Wet</i>	2.56	-127	108	1.9x10 ¹⁹	10	977	56.4
<i>T_p 1500, Crust 45 km, Wet</i>	3.23	-52	62	8.9x10 ¹⁸	11	1041	93.1
<i>T_p 1550, Crust 45 km, Wet</i>	1.67	-128	61	4.0x10 ¹⁹	13	1033	33.23
<i>T_p 1550, Crust 45 km, Wet</i>	1.59	122	85	9.9x10 ¹⁸	13	1036	189
<i>T_p 1550, Crust 45 km, Wet</i>	1.59	369	73	1.4x10 ¹⁹	15	1061	175
<i>T_p 1550, Crust 45 km, Wet</i>	1.63	-318	82	9.5x10 ¹⁸	15	1078	290
<i>T_p 1650, Crust 45 km, Dry</i>	4.32	-127	139	1.4x10 ¹⁹	15	1039	336
<i>T_p 1650, Crust 45 km, Dry</i>	4.33	355	127	5.3x10 ¹⁹	15	1031	81
<i>T_p 1650, Crust 45 km, Dry</i>	4.47	330	152	3.0x10 ¹⁸	20	1162	4056
<i>T_p 1650, Crust 45 km, Dry</i>	4.48	-80	172	2.6x10 ¹⁸	20	1173	5231
<i>T_p 1650, Crust 45 km, Dry</i>	4.69	300	130	1.9 x10 ¹⁹	25	1096	986
<i>T_p 1600, Crust 45 km, Dry</i>	3.32	-80	121	2.5x10 ²⁰	13	1027	11
<i>T_p 1600, Crust 45 km, Dry</i>	3.46	379	125	8.6x10 ¹⁹	15	1046	49
<i>T_p 1600, Crust 45 km, Dry</i>	3.78	270	148	1.1x10 ²⁰	17	1027	64
<i>T_p 1550, Crust 45 km, Dry</i>	3.53	-310	31	5.7x10 ¹⁹	14	1049	15
<i>T_p 1550, Crust 45 km, Dry</i>	3.53	122	126	5.1x10 ¹⁹	15	1095	83
<i>T_p 1600, Crust 25 km, Dry</i>	5.20	-68	165	1.4x10 ¹⁹	17	1147	566
<i>T_p 1600, Crust 25 km, Wet</i>	3.01	260	132	2.5x10 ¹⁸	12	1094	927
<i>T_p 1600, Crust 25 km, Wet</i>	3.12	-190	89	1.3x10 ¹⁹	7	978	23

Table S2. Measured parameters at the onset of a dripping instability from the numerical simulations. Black colors indicate the first dripping instabilities that occur in the model. Red colors indicate drips that form at a later stage. In most cases these instabilities form over significant upwellings.

The results indicate that the onset of the first instabilities is well captured with the expression for R_b given above, provided that a value for C of 0.1 is used, after which drips are predicted to develop as soon as $R_b > 1$. Later instabilities commonly form above the larger partially molten upwellings. In this case, the velocity of the drips has to be not only faster than diffusion but also faster than the upward motion of the isentropically melting mantle. As a result, the condition $R_b > 1$ is insufficient and $R_b > 100$ is typically required.

The simple scaling law may be used to obtain insight into the maximum viscosity and minimum layer thicknesses that are required for a drip to develop at the Moho. Solving for H gives

$$H = \left(\frac{R_{b,crit} \kappa \eta}{C \Delta \rho g} \right)^{\frac{1}{3}}$$

where $R_{b,crit}$ is the critical number (between 1 and 100 for most of the experiments), $C = 0.1$, and all other parameters as described above. Figure S13 shows a comparison of the analytical predictions with the numerical results at the onset of dripping. The agreement is reasonable and shows that a hot mantle lithosphere, which has smaller effective viscosities, will develop smaller drips. As the surface/volume ratio of smaller drips is larger, we expect them to heat in an efficient manner and therefore potentially melt (cf. Elkins-Tanton, 2005).

Our results indicate that layers thinner than 5 km would need a very low viscosity to become negatively buoyant and drip-off, or, alternatively, they would need to be thickened by another process (for example, by an adjacent hot upwelling). Yet, once a drip starts going, our simplified analysis strongly underestimates the velocity of the drips, and numerical simulations show that the resulting drips take most of the negatively buoyant crustal material with them into the mantle. This is the reason that nearly all of the negatively buoyant crust disappears. The stable crust does *not* disappear into the mantle (there is almost no “dark blue” material present in the mantle in the snapshots from the experiments), which further supports our interpretation that the lower crust is indeed removed by RT instabilities. Both positive and negatively buoyant “new” crust is coloured green; the negatively buoyant crust sinks into the mantle through the same mechanism where it is likely to melt as discussed in the main text.

The effect of phase transitions on dynamics of the early Earth has been discussed before. Particularly, Davies (1992) conjectured that the basalt–eclogite transition could play a role by adding negative buoyancy to a plate with a thick crust and thereby add to the negative buoyancy of those plates. Yet, he concluded that:

“It is quite possible that the effect of the basalt–eclogite transformation could have increased the rate of plate tectonics, but perhaps not dramatically and only intermittently” (Davies, 1992).

Our models show that the phase transitions indeed play a major role in the early Earth. Yet, rather than extending the plate-tectonics regime by adding additional negative buoyancy, the phase transitions help to drive rapid crustal recycling of an Earth that was otherwise in the drip tectonics mode. The exact physics of why the Earth switched from a drip-tectonics to a plate-tectonics regime remains to be understood, but our models do suggest that petrological constraints should be taken into account in such models.

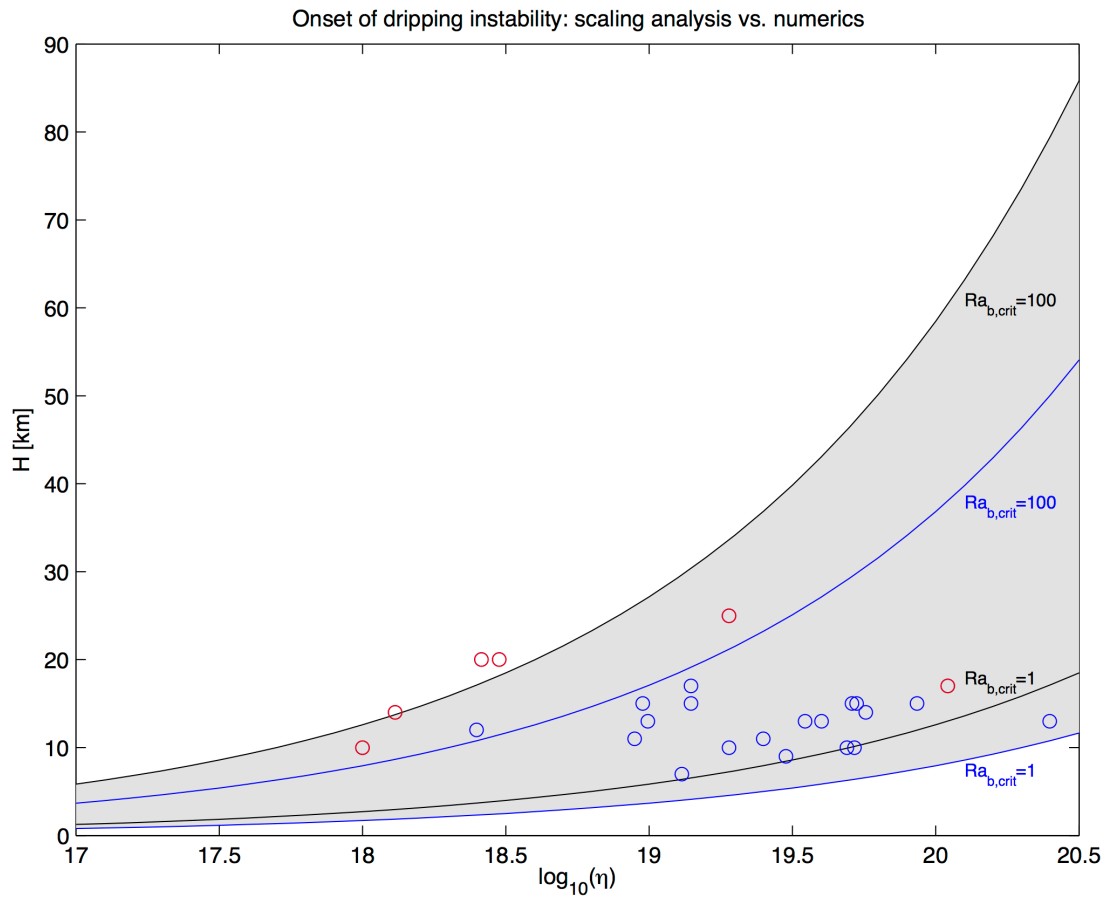


Figure S13: Analytical predictions for the minimum negatively buoyant layer thickness as a function of viscosity that is required for a dripping instability to develop (for this $Ra_b > 1$). Solid lines are predictions assuming $\Delta\rho=50$ (black lines) and $\Delta\rho=200 \text{ kg/m}^3$ (blue lines). Circles are the results from the numerical simulations, where blue indicate the first drips that form in the simulations and red circles indicate drips that form at a later stage (typically above large scale upwellings). The agreement is quite reasonable given the simplicity of the scaling analysis, and shows that only small drips will form in a hotter mantle (which has a lower viscosity).

4. References

- Ahmad, T., Dragusanu, C. & Tanaka, T. Provenance of Proterozoic Basal Aravalli mafic volcanic rocks from Rajasthan, Northwestern India: Nd isotopes evidence for enriched mantle reservoirs. *Precambrian Res.* **162**, 150–159 (2008).
- Balakrishnan, S., Rajamani, V., Hanson, G. N. U-Pb ages for zircon and titanite from the Ramagiri area, southern India: Evidence for accretionary origin of the eastern Dharwar craton during the late Archean. *J. Geology* **107**, 69–86 (1999).
- Berry, A. J., Danyushevsky, L. V., O'Neill, H. St C., Newville, M. & Sutton, S. R. Oxidation state of iron in komatiitic melt inclusions indicates hot Archean mantle. *Nature* **455**, 960–963 (2008).
- Bittner, D. & Schmeling, H. Numerical modelling of melting processes and induced diapirism in the lower crust. *Geophys. J. Int.* **123**, 59–70 (1995).
- Brown, M. Metamorphic conditions in orogenic belts: A record of secular change. *Int. Geol. Rev.* **49**, 193–234 (2007).
- Card, K. D. A review of the Superior province of the Canadian shield, a product of Archean accretion. *Precambrian Res.* **48**, 99–156 (1990).
- Carter, N. L. & Tsenn, M. C. Flow properties of continental lithosphere. *Tectonophysics.* **136**, 27–63 (1987).
- Connolly, J. A. D. Computation of phase equilibria by linear programming: a tool for geodynamic modeling and its application to subduction zone decarbonation. *Earth Planet. Sci. Lett.* **236**, 524–541 (2005).
- Conrad, C. & Molnar, P. The growth of Rayleigh–Taylor-type instabilities in the lithosphere for various rheological and density structures. *Geophys. J. Int.* **129**, 95–112 (1997).
- Crameri, F. & Kaus, B. Parameters that control lithospheric-scale thermal localization on terrestrial planets. *Geophys. Res. Lett.* **37**, Article Number: L09308 (2010).
- Crameri, F. *et al.* A comparison of numerical surface topography calculations in geodynamic modelling: an evaluation of the ‘sticky air’ method. *Geophys. J. Int.* **189**, 38–54 (2012).
- Dabrowski, M., Krotkiewski, M. & Schmid, D. W. MILAMIN: MATLAB-based finite element method solver for large problems. *Geochemistry, Geophysics, Geosystems* **9**, Article Number: Q04030 (2008).
- Davies, G. On the Emergence of Plate-Tectonics. *Geology* **20**, 963–966 (1992).
- Deubelbeiss, Y., Kaus, B. & Connolly, J. A. D. Direct numerical simulation of two-phase flow: Effective rheology and flow patterns of particle suspensions. *Earth Planet. Sci. Lett.* **290**, 1–12 (2010).

- Diener, J. F. A. & Powell, R. Revised activity-composition relations for clinopyroxene and amphibole. *J. Metamorph. Geol.* **30**, 131–142 (2012).
- Elkins-Tanton, L. T. Continental magmatism caused by lithospheric delimitation. In Foulger, G. R., Natland, J. H., Presnall, D. C. & Anderson, D. L. (eds) *Plates, Plumes, and Paradigms*, Geological Society of America Special Paper 388, 449–461 (2005).
- Gerya, T. V. & Yuen, D. A. Robust characteristics method for modelling multiphase visco-elasto-plastic thermo-mechanical problems. *Phys. Earth Planet. Int.* **163**, 83–105 (2007).
- Ghiorso, Mark S., Hirschmann, Marc M., Reiners, Peter W., & Kress, Victor C. III The pMELTS: An revision of MELTS aimed at improving calculation of phase relations and major element partitioning involved in partial melting of the mantle at pressures up to 3 GPa. *Geochemistry, Geophysics, Geosystems* **3**, Article Number: 1030 (2002).
- Green, M. G., Sylvester, P. J. & Buick, R. Growth and recycling of early Archaean continental crust: geochemical evidence from the Coonterunah and Warrawoona Groups, Pilbara Craton, Australia. *Tectonophys.* **322**, 69–88 (2000).
- Herzberg, C., Condie, K. & Korenaga, J. Thermal history of the Earth and its petrological expression. *Earth Planet. Sci. Lett.* **292**, 79–88 (2010).
- Hirth, G. & Kohlstedt, D. Rheology of the upper mantle and the mantle wedge: A view from the experimentalists. In J. Eiler (ed) *Inside the Subduction Factory*, Geophysical Monograph American Geophysical Union, Washington, D.C. **138**, 83–105 (2003).
- Holland T. J. B. & Powell R. An internally consistent thermodynamic data set for phases of petrological interest. *J. Metamorph. Geol.* **16**, 309–43 (1998).
- Holland, T. J. B. & Powell. R. Activity-composition relations for phases in petrological calculations: an asymmetric multicomponent formulation. *Contrib. Mineral. Petrol.* **145**, 492–501 (2003).
- Kato, Y. & Nakamura, K. Origin and global tectonic significance of Early Archean cherts from the Marble Bar greenstone belt, Pilbara Craton, Western Australia. *Precambrian Res.* **125**, 191–243 (2003).
- Katz, R. F., Spiegelman, M. & Langmuir, C. H. A new parameterization of hydrous mantle melting. *Geochemistry, Geophysics, Geosystems* **4**, Article Number: 1073 (2003).
- Kaus, B. Factors that control the angle of shear bands in geodynamic numerical models of brittle deformation. *Tectonophys.* **484**, 36–47 (2010).
- May, D. A. & Moresi, L. Preconditioned iterative methods for Stokes flow problems arising in computational geodynamics. *Phys. Earth Planet. Int.* **171**, 33–47 (2008).
- Polat, A. *et al.* The origin and compositions of Mesoarchean oceanic crust: Evidence from the 3075 Ma Ivisartoq greenstone belt, SW Greenland. *Lithos* **100**, 293–321 (2008).

Schmeling, H. *et al.* A benchmark comparison of spontaneous subduction models--Towards a free surface. *Phys. Earth Planet. Int.* **171**, 198–223 (2008).

Shchipansky, A. A. *et al.* 2.8 Ga boninite-hosting partial suprasubduction zone ophiolite sequences from the north Karelian greenstone belt, NE Baltic shield, Russia. In Kusky, T.M., ed., Precambrian ophiolites and related rocks. Elsevier B.V., *Developments in Precambrian geology* **13**, 425–486 (2004).

Sizova, E., Gerya, T., Brown, M. & Perchuk, L. Subduction styles in the Precambrian: Insight from numerical experiments. *Lithos* **116**, 209–229 (2010).

Smithies, R. H., Van Kranendonk, M. J. & Champion, D. C. It started with a plume - early Archaean basaltic proto-continental crust. *Earth Planet. Sci. Lett.* **238**, 284–297 (2005).

St-Onge, M. R., Lucas, S. B., Scott, D. J. & Wodicka, N. Upper and lower plate juxtaposition, deformation and metamorphism during crustal convergence, Trans-Hudson Orogen (Quebec-Baffin segment), Canada. *Precambrian Res.* **93**, 27–49 (1999).

Tackley, P. J. & King, S. D. Testing the tracer ratio method for modeling active compositional fields in mantle convection simulations. *Geochemistry, Geophysics, Geosystems* **4**, Article Number: 8302 (2003).

Thielmann, M. & Kaus, B. Shear heating induced lithospheric-scale localization: Does it result in subduction? *Earth Planet. Sci. Lett.* **359-360**, 1–13 (2012).

Volpe, A. M. & Macdougall, J. D. Geochemistry and isotopic characteristics of mafic (Phulad ophiolite) and related rocks in the Delhi-Supergroup, Rajasthan, India - implications for rifting in the Proterozoic. *Precambrian Res.* **48**, 167–191 (1990).

Wang, X. C., Li, X. H., Li, W. X. & Li, Z. X. Ca. 825 Ma komatiitic basalts in South China: First evidence for >1500°C mantle melts by a Rodinian mantle plume. *Geology* **35**, 1103–1106 (2007).

White, R. W., Powell, R. & Clarke, G. L. The interpretation of reaction textures in Fe-rich metapelitic granulites of the Musgrave Block, central Australia: Constraints from mineral equilibria calculations in the system K₂O–FeO–MgO–Al₂O₃–SiO₂–H₂O–TiO₂–Fe₂O₃. *J. Metamorph. Geol.* **20**, 41–55 (2002).

White, R. W., Powell, R. & Holland T. J. B. Progress relating to calculation of partial melting equilibria for metapelites. *J. Metamorph. Geol.* **25**, 511–527 (2007).

White, R. W., Powell, R., Holland, T. J. B. & Worley, B. The effect of TiO₂ and Fe₂O₃ on metapelitic assemblages at greenschist and amphibolite facies conditions: mineral equilibria calculations in the system K₂O–FeO–MgO–Al₂O₃–SiO₂–H₂O–TiO₂–Fe₂O₃. *J. Metamorph. Geol.* **18**, 497–511 (2000).

Yamato, P., Kaus, B., Mouthereau, F. & Castellort, S. Dynamic constraints on the crustal-scale rheology of the Zagros fold belt, Iran. *Geology* **39**, 815–818 (2011).